A failure of climate models to simulate aeolian dust

Amato T. Evan*[1,2], Cyrille Flamant[2], Stephanie Fiedler[3], Owen Doherty[1]

[1]Scripps Institution of Oceanography, University of California San Diego, La Jolla, California, USA.

[2]Laboratoire Atmosphère, Milieux, Observations Spatiales, CNRS and Université Pierre et Marie Curie, Paris, France.

[3]School of Earth and Environment, University of Leeds, LS2 9JT Leeds, UK

*Correspondence to: aevan@ucsd.edu

First Paragraph

The emission and transport of aeolian dust is both influenced by–and influences–the Earth's climate. Dust emission is controlled by terrestrial processes and atmospheric winds, the latter of which is also responsible for subsequent transport (1–3). Suspended dust radiatively cools the surface and warms the atmosphere via direct and indirect effects (3–5), in-turn altering regional winds and rainfall (6,7) and consequently the dust cycle. Dust is an external source of nutrients to the oceans and remote terrestrial ecosystems (8,9) and alters the global carbon cycle (10). Therefore, with respect to simulations of the climate by models, biases in the dust cycle likely result in biases in modeled energy and nutrient budgets and the hydrological cycle, yet the representation of dust in state-of-the-art climate models has not been systematically evaluated. Here we assess African dust in 23 state-of-the-art global climate models used in the Fifth Assessment Report of the Intergovernmental Panel on Climate Change. We find that all models fail to reproduce basic aspects of the dust cycle. Models systematically underestimate dust emission, transport and optical depth, and year-to-year changes in these properties bear little resemblance to observations. These findings cast doubt on the ability of these models to accurately simulate regional climate variability and future change.

Main text

A major limitation in evaluating aeolian dust in climate models is the lack of high quality and long-term measurements of dust. Satellite retrievals from which a dust concentration can be derived extend back to approximately 1980, but these data have uncertainties (11,12). Surface measurements of visibility can go back even further, but these are not purely indicative of dust aerosol, nor are they always homogeneous in time (13). High temporal resolution proxy records of atmospheric dust are also a source of estimates of historical concentrations, but to-date these data are few (12). Despite these shortcomings of existing mineral aerosol observations, there are a few robust data sets against which models can be evaluated. Among these we focus on observations indicating dust emission and transport from northern Africa, the world's largest dust source (14). We first examine the long-term mean dust aerosol concentration west of northern Africa over which dust is predominantly exported, 10°-20°N and 20°-30°W. We specify this region since it includes the island nation of Cape Verde for which a long proxy record of dust exists (12). However, expanding this region eastward or northward has no substantive effect on the results presented here.

We compare the distributions of the annual mean dust mass path (DMP; g m^{-2}), which is the vertically integrated mass of atmospheric dust per unit area, from the Fifth Assessment Report of the Intergovernmental Panel on Climate Change (CMIP5) models (Table S1) against satellite retrievals of DMP from the Advanced Very High Resolution Radiometer (AVHRR) (15, 16) for 1982-2004 and the Moderate Resolution Imaging Spectroradiometer (MODIS) (17,18) Terra instrument for 2000–2013. The ensemble mean DMP is calculated from the CMIP5 20th Century historical simulations for which this output is available (Table S1). Satellite retrieved DMP is calculated from retrievals of aerosol optical depth (τ) and via measurements of the ratio of DMP to the portion of the optical depth that is due to dust (τ_d) (Table 1) following Kaufman et al. (19) (see Methods).

The multi-model ensemble highlights a median DMP of 0.24 g m^{-2}, with model medians spanning 0.05 to 0.46 g m^{-2} (Fig 1a). In contrast, the median DMPs from the AVHRR and MODIS retrievals is 0.75 and 0.82 g m^{-2}, respectively, which is a factor of three larger than the multi-model median. Compared against individual models the satellite retrieved DMP is larger by a factor of two (CCSM) to 12 (MIROC4h). In addition, most CMIP5 models underestimate the width of the interquartile range, which is not surprising given the low bias in the mean state. However, we note that some models exhibit a very small range in DMP (*e.g.*, the IPSL models) because there is no year-to-year change in the modeled dust emission (*i.e.*, emission is prescribed), and thus changes in DMP are due to variations in advection and deposition only.

To elucidate the source of the low bias in modeled dust mass path, we calculated the long-term mean total dust emission from northern Africa (Tg) (Fig 1b), for the models for which emission data is available (Table S1). DMP over the tropical North Atlantic is directly proportional to the total northern African dust emission, where the slope of the linear regression is 1.64±0.85 x 10^{-5} g m^{-2} per Tg (Fig 1a, red line) (the uncertainty

represents the 95% confidence interval on the slope of the fit). Thus, the biases in Figure 1a are likely related to processes affecting emission, and less to modeled transport and deposition. If we estimate the total emission from northern Africa based on the linear fit between models' emission and mass path, but using the average mass path values from the satellites (Fig 1a), northern African dust emission is approximately 4500 Tg per year (Fig 1b, inset), a factor of three greater than the multi-model mean emission from CMIP5 (Fig 1a).

As observations of total northern African emission are not available there is no way to evaluate the accuracy of the model output or the satellite-based estimates. Thus, while the range of model values seen here is consistent with other analysis of model output (20,21), there is no a priori reason to reject the satellite estimates as being biased high. Kok (22) found that the size distribution of dust at emission was biased towards small particles causing larger optical depth per unit mass (τ) and speculated that the resulting dust mass emitted is underestimated by a factor of two to eight. This may be an artifact of tuning the models to τ observations, and we find a very good agreement in the mean τ between the model ensemble of 0.38 and the satellite retrievals of 0.34 (Table 1).

However, τ is the sum of the contributions from different aerosol species broadly categorized as marine (τ_{ma}), anthropogenic (τ_{an}) and dust (τ_d). MODIS retrievals of fine mode τ (17), nominally PM1.0, enable the separation of the MODIS and AVHRR τ into these three components (12, 19). Several of the CMIP5 models also output fine mode τ (Table S1), and thus we are able to use the same methodology in Ref. 19 to separate the models' τ into these components (see Methods). The comparison of modeled and satellite retrieved τ_d shows less agreement than that for τ; the mean satellite retrieved τ_d is 0.30 and the multi model mean τ_d is 0.22 (Table 1). Eight CMIP5 models have a lower τ_d (minimum of 0.09) that the satellites, one model has a higher τ_d (0.35), and two models have mean τ_d that is not statistically different from MODIS. For the three models in which τ_d is greater or equal to the satellite retrieved τ_d (both MIROC models and the CSIRO-Mk3), the total DMP bias (Fig 1a) can be prescribed to the size distribution of the emitted dust being too skewed towards small particles as proposed in Ref. 19. In the majority of models with smaller τ_d than the satellite retrievals, the DMP bias can be related to both the emitted size distribution and an underestimation of the total amount of dust emitted from northern Africa (which may be due to insufficient mass emitted per dust emission event, or a lack of sufficient events), where the percentage of the error due to the skewed size distribution is $100\% \times min\{1, \tau_{\mathrm{d,MODEL}}/\tau_{\mathrm{d,MODIS}}\}$, and the percentage of the error that is due to an insufficient total flux is 100% minus this value. From these calculations, and averaged across all models, 66% of the bias in DMP (Fig 1a) is due to a bias in the emitted size distribution ("Size bias" in Table 1), and 34% of the bias in DMP is due to an underestimation of total northern African emission ("Flux bias" in Table 1).

The low biases in emission (Fig 1b) likely result from a number of factors, ranging from soil moisture content to vegetation cover to near surface wind speed distributions. In an attempt to elucidate the causes of the model biases in emission and thus DMP we

examined the spatial structure of surface emission across northern Africa in comparison to a satellite-derived map of emission frequency (Fig S1). Although the analysis did not provide any obvious clues for the causes of the biases, the level of disagreement between the models, and to observations, was stark, suggesting that the biases in emission likely result for a variety of reasons that are not necessarily consistent among the models.

We also examined the time evolution of DMP from CMIP5 models to evaluate the interannual variability. Here we use a hybrid satellite-paleo record of annual mean τ_d corresponding to a location adjacent to the Cape Verde islands (15°N & 23°W) that spans 1955–2009 (12; Fig 2a), and compute mass path in a manner identical to that for the AVHRR data in Figure 1a (12). One major feature of the observational time series is the increase of τ_d over the tropical North Atlantic from the 1950s through the early 1980s, and then a subsequent decline of emission and τ_d through the 2000s (Fig 2a), which is documented in satellite and in-situ data sets (10,12,23,24). Although the cause of these trends is still debatable, there is consensus that they are either directly or indirectly caused by the simultaneous changes in summertime Sahelian rainfall, and in particular the severe drought of the 1980s (10,24,25).

We regressed a time series of observed June–September averaged Sahelian rainfall rates (26) onto the proxy record of DMP to quantify this dependency for 1960–2004.The observed coefficient of the regression is -0.06±0.04 g m^{-2} per mm day^{-1}, which is statistically different from zero at the 95% significance level (Fig 2b). Using the models' rainfall rates and DMP for the same years (Fig 2b), only the MIROC-ESM-CHEM has a negative regression coefficient statistically different from zero at the 95% level (Fig 2b). Consistent with our findings, a recent study found that a subset of the models evaluated here exhibited a negative correlation between DMP over the tropical North Atlantic and the phase of the modeled AMO in 20th Century historical forcing runs, although the change was not determined to be statistically significant (28).

We also compared annual mean DMP from observations (AVHRR) to model output for the AMIP simulations for the years 1982–2006 via a Taylor diagram (29) (Fig 2c). The two striking features are that (1) none of the models (B-L in Fig 2c) exhibit a statistically significant positive correlation to the data (A in Fig 2c), with multi-model mean and median correlation coefficients smaller than zero, and that (2) the root-mean-squared biases are similar in magnitude to the observational data's standard deviation. Similar results are found with the proxy DMP data and model output for the historical forcing runs for 1960–2004 (Fig S2).

Based on the results presented here CMIP5 models are unable to capture any of the salient features of northern African dust emission and transport. As such, there is no reason to assume that the projections of dust aerosol for the 21st Century emissions have any validity. Despite highlighting deficiencies in the representation of the multitude of land and atmospheric processes that govern dust emission, these results also cast doubt on the representation of other features of coupled Earth system that are affected by aeolian dust, including regional land and ocean surface temperatures,

precipitation processes, and terrestrial and oceanic biogeochemistry. It is likely that the representation of dust in climate models can be improved by increasing observations of processes affecting dust emission in the remote dryland regions where most dust storms occur.

Methods

Estimating DMP from satellites

MODIS retrieved and CMIP5 output total aerosol optical depth and fine mode optical depth were converted to τ_d via Ref 19. AVHRR retrievals of total aerosol optical depth were converted to τ_d via Ref 12, which is an application of the Ref. 19 methodology to this instrument. We note that for the CMIP5 models the fine mode fractions for anthropogenic, mineral and marine aerosols were nearly identical to the values reported in Ref 19. For the satellites, τ_d data was converted to DMP via the ratio of 2.7 g m^{-2} per unit τ_d (Table 1), which is based on the average of observations of this ratio (19). Two models (CCSM and CESM) only report τ_d and not DMP, therefore we calculated the ratio of τ_d to DMP for this model using the CESM total aerosol mass fields in an over-water area where the aerosol loading is dominated by dust (2.2 g m^{-2} per unit τ_d; Table 1). However, the inclusion of marine aerosols in the total aerosol mass field means that the value of 2.2 is an upper bound on the actual ratio for the model, and that the τ_d estimates for CCSM and CESM are likely to be biased high.

References

1. Marticorena, B., and G. Bergametti (1995), Modeling the atmospheric dust cycle: 1. Design of a soil-derived dust emission scheme, J. Geophys. Res., 100(D8), 16415–16430, doi:10.1029/95JD00690.
2. Shao, Y., Wyrwoll, K. H., Chappell, A., Huang, J., Lin, Z., McTainsh, G. H., ... & Yoon, S. (2011). Dust cycle: An emerging core theme in Earth system science. Aeolian Research, 2(4), 181-204.
3. Tegen, I., A. A. Lacis and I. Y. Fung, 1996. The influence of mineral aerosol from disturbed soils on the global radiation budget. Nature, 380, 419‑422.
4. Evan, A. T., D. J. Vimont, R. Bennartz, J. P. Kossin and A. K. Heidinger (2009) The role of aerosols in the evolution of tropical North Atlantic Ocean temperature, Science, Vol. 324. no. 5928, pp. 778 - 781.
5. Kaufman, Y. J., I. Koren, L. A. Remer, D. Rosenfeld, and Y. Rudich, 2005: The effect of smoke, dust, and pollution aerosol on shallow cloud development over the Atlantic Ocean. Proc. Natl. Acad. Sci, 102, 11207–11212.
6. Evan, A. T., G. R. Foltz, D. Zhang, and D. J. Vimont, 2011: Influence of African dust on ocean–atmosphere variability in the tropical Atlantic. Nat. Geosci., 4, 762–765, doi:10.1038/ngeo1276.
7. Yoshioka, M., N. M. Mahowald, A. J. Conley, W. D. Collins, D. W. Fillmore, C. S. Zender, and D. B. Coleman, 2007: Impact of desert dust radiative forcing on Sahel precipitation: Relative importance of dust compared to sea surface temperature variations, vegetation changes, and greenhouse gas warming. J. Climate, 20, 1445–1467.
8. Das, R., A. T. Evan and D. Lawrence (2013) Contributions of long-distance dust transport to atmospheric P inputs in the Yucatan Peninsula, Global Biogeo. Cycles, 27, 167–175.
9. Okin, G. S., et al. (2011), Impacts of atmospheric nutrient deposition on marine productivity: Roles of nitrogen, phosphorus, and iron, Global Biogeochem. Cycles, 25, GB2022, doi:10.1029/2010GB003858.
10. Mahowald, N. M., et al.: Observed 20th century desert dust variability: impact on climate and biogeochemistry, Atmos. Chem. Phys., 10, 10875-10893, doi:10.5194/acp-10-10875-2010, 2010.
11. Engelstaedter, S., and R. Washington (2007), Atmospheric controls on the annual cycle of North African dust, J. Geophys. Res., 112, D03103, doi:10.1029/2006JD007195.
12. Evan, A. T., S. Mukhopadhyay, 2010: African Dust over the Northern Tropical Atlantic: 1955–2008. J. Appl. Meteor. Climatol., 49, 2213–2229.
13. Mahowald, N. M., Ballantine, J. A., Feddema, J., and Ramankutty, N.: Global trends in visibility: implications for dust sources, Atmos. Chem. Phys., 7, 3309-3339, doi:10.5194/acp-7-3309-2007, 2007.
14. Washington, R., Todd, M., Middleton, N. J. and Goudie, A. S. (2003), Dust-Storm Source Areas Determined by the Total Ozone Monitoring Spectrometer and Surface

Observations. Annals of the Association of American Geographers, 93: 297–313. doi: 10.1111/1467-8306.9302003.
15. Stowe, L. L., A. M. Ignatov, and R. R. Singh, 1997: Development, validation, and potential enhancements to the second generation operational aerosol product at the National Environmental Satellite, Data, and Information Service of the National Oceanic and Atmospheric Administration. J. Geophys. Res., 102 (D14), 16 923–16 934.
16. AVHRR data from the National Oceanic and Atmospheric Administration National Climatic Data Center at http://www.ncdc.noaa.gov/cdr/operationalcdrs.html.
17. Remer, L. A., and Coauthors, 2005: The MODIS Aerosol Algorithm, Products, and Validation. J. Atmos. Sci., 62, 947–973.
18. MODIS data from the Giovanni online data system, developed and maintained by the NASA GES DISC at http://disc.sci.gsfc.nasa.gov/giovanni.
19. Kaufman, Y. J., I. Koren, L. A. Remer, D. Tanre´, P. Ginoux, and S. Fan, 2005: Dust transport and deposition observed from the Terra-Moderate Resolution Imaging Spectroradiometer (MODIS) spacecraft over the Atlantic Ocean. J. Geophys. Res., 110, D10S12, doi:10.1029/2003JD004436.
20. Engelstaedter, S., Tegen, I. and Washington, R., 2006. North African dust emissions and transport. Earth-Science Reviews 79(1-2), 73-100.
21. Huneeus, N. et al.: Global dust model intercomparison in AeroCom phase I, Atmos. Chem. Phys., 11, 7781-7816, doi:10.5194/acp-11-7781-2011, 2011.
22. Kok, J. F.: A scaling theory for the size distribution of emitted dust aerosols suggests climate models underestimate the size of the global dust cycle, Proc. Natl. Acad. Sci. USA, 108, 1016–1021, 2011.
23. Foltz, G. R., and M. J. McPhaden (2008), Trends in Saharan dust and tropical Atlantic climate during 1980–2006, Geophys. Res. Lett., 35, L20706, doi:10.1029/2008GL035042.
24. Prospero, J. M., & Lamb, P. J. (2003). African droughts and dust transport to the Caribbean: Climate change implications. Science, 302(5647), 1024-1027.
25. Cowie SM; Knippertz P; Marsham JH (2013) Are vegetation-related roughness changes the cause of the recent decrease in dust emission from the Sahel?, Geophysical Research Letters, 40, pp.1868-1872.
26. Sahel precipitation data from the Joint Institute for the Study of the Atmosphere and Ocean, doi: 10.6069/H5MW2F2Q. Sahel averaging regions are from Ref 27.
27. Janowiak, J. E., 1988: An investigation of interannual rainfall variability in Africa. J. Climate, 1, 240-255.
28. Martin, Elinor R., Chris Thorncroft, Ben B. B. Booth, 2014: The Multidecadal Atlantic SST—Sahel Rainfall Teleconnection in CMIP5 Simulations. *J. Climate*, **27**, 784–806.
29. Taylor, K. E. (2001), Summarizing multiple aspects of model performance in a single diagram, J. Geophys. Res., 106(D7), 7183–7192, doi:10.1029/2000JD900719.

Acknowledgements

We acknowledge Ian Eisenman and Kerstin Schepanski for comments on the methodologies and the satellite emission map used in this study. This work was supported by the french Agence Nationale de la Recherche (ANR) grant ANR-10-LABX-18-01 of the national Programme Investissements d'Avenir. Funding for this work was also provided by Laboratoire d'excellence Institute Pierre Simon Laplace (L-IPSL), a grant from the "Research in Paris" programme, and National Oceanographic and Atmospheric Administration Climate Program Office grant NA11OAR4310157.

Author Contributions

A.E. and C.F. designed the study. O.D. and S.F. provided the data used here. A.E. prepared all figures. All authors contributed to data analysis and manuscript preparation.

Competing Financial Interests Statement

There are no competing financial interests.

Figure Legends

Figure 1a. Long-term mean dust emission and mass path from satellite retrievals and CMIP5 models. Shown (1a) are box-and-whisker plots of the long-term annual mean dust mass path over the region 10°-20°N and 20°-30°W. Medians (red lines), interquartile range (blue boxes), the interquartile value +/- 1.25 times the interquartile range (black "whiskers") and outliers (red crosses) are calculated from annual mean dust mass path values over the period 1982–2004 (2000–2013 for the MODIS-Terra data). The model-averaged median mass path is 0.26 g m^{-2} (red line), which is a factor of three smaller than the satellite-derived dust mass path medians of 0.75 g m^{-2} (AVHRR) and 0.82 g m^{-2} (MODIS). Also shown (1b) is a scatterplot of annual mean DMP averaged over 10°-20°N and 20°-30°W (ordinate) and mean annual total dust emission from northern Africa (abscissa), for CMIP5 models (main plot) and the AVHRR and MODIS (inset), where error bars indicate the ± 1σ range of these data. Among the CMIP5 models the correlation coefficient of DMP and emission is 0.86 (p-value < 0.01) and the linear least square best fit line is $y = x \times 1.6e^{-4} + 0.05$ (red line), where the slope of the fit is statistically different from zero (p-value < 0.01). Annual mean dust emission values for the satellite data are estimated via this best-fit line.

Figure 2. Annual variability of modeled and observed dust. Plotted in 3a are the proxy and AVHRR annual mean time series of τ_d averaged over 10°-20°N and 20°-30°W. Plotted in 3b are the coefficients (filled circles) and their 95% certainty levels (bars) from the regression of AVHRR and modeled DMP onto observed (for the AHVRR only) and modeled June–September Sahelian rainfall (10°-20°N and 15°W–20°E), calculated with data from 1960–2004. In 3c is a Taylor diagram for annual mean DMP for 1960–2004 and averaged over 10°-20°N and 20°-30°W. The red circle marked "A" represents the proxy record of DMP (3c), and the other markers are CMIP5 models (see Table S1 for legend). The abscissa and dotted black semi-circles represent the time series' standard deviation, the dashed green semi-circles are the root mean squared differences between the models and the proxy record, and the radial blue dot-dashed lines are the correlation coefficients of the model time series and the proxy record.

Tables

	τ	τ_d	Size bias (%)	Low Flux bias (%)	DMP/τ_d
AVHRR	0.38	0.29	-	-	2.7
MODIS	0.38	0.30	-	-	2.7
CSIRO-Mk3	0.40	0.33	100	0	1.3
GFDL-CM3	0.33	0.13	45	55	1.5
GFDL-ESM2G	0.32	0.22	73	27	1.6
GFDL-ESM2M	0.32	0.22	74	26	1.6
IPSL-CM5A-LR	0.30	0.17	55	45	1.4
IPSL-CM5A-MR	0.31	0.17	56	44	1.4
IPSL-CM5B-LR	0.30	0.16	54	46	1.4
MIROC-ESM-CHEM	0.48	0.35	100	0	1.3
MIROC-ESM	0.48	0.35	100	0	1.3
MRI-CGCM3	0.25	0.09	31	69	3.4
MRI-ESM1	0.26	0.10	33	67	2.7
Multi-model	**0.34**	**0.22**	**66**	**34**	**1.7**

Table 1. Satellite and model long-term mean optical depth statistics. Shown in the 2nd and 3rd columns are the long-term mean τ and τ_d for AVHRR (1982–2005) and MODIS (2001–2012), and CMIP5 models (1982–2005) for which fine model optical depth data was available. Here the model mean optical depths that are greater than or less than that from both satellites are shaded red and blue, respectively, at the 95% significance level. The 4th and 5th columns are estimates of the percentage of the DMP biases (Fig 1a) that are due to biases in the size distributions of the emitted dust and the biases in the total flux of dust emitted from northern Africa. The last column is the observational (for AVHRR and MODIS) and model estimated ratio of DMP to τ_d.

Figures

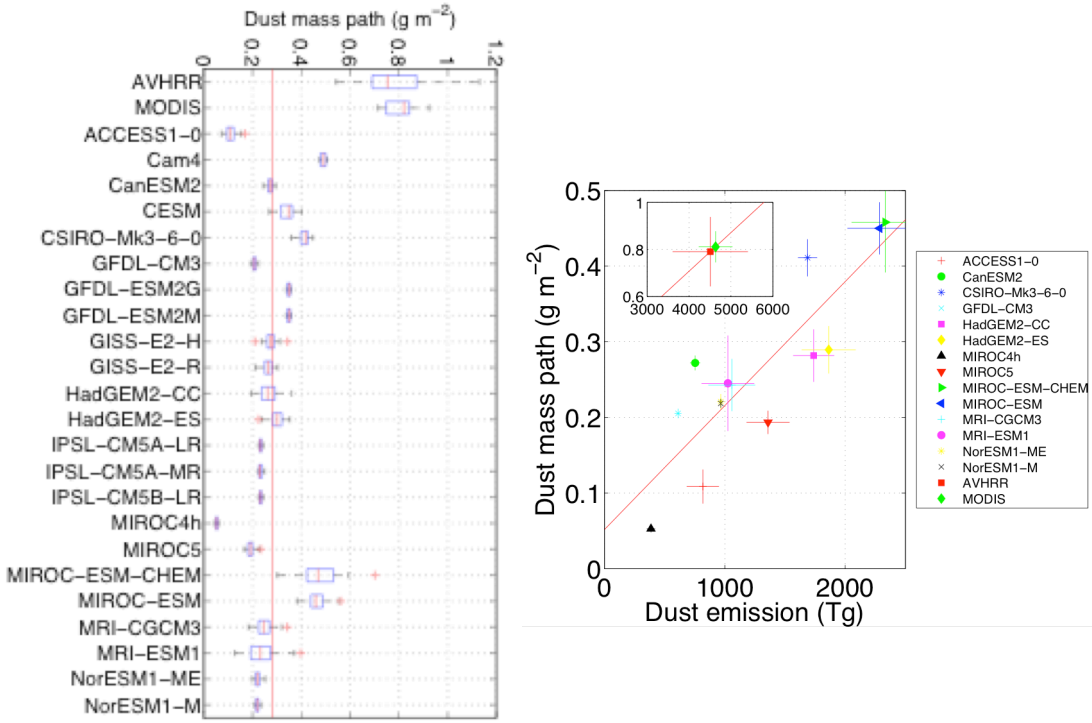

Figure 1a. Long-term mean dust emission and mass path from satellite retrievals and CMIP5 models. Shown (1a) are box-and-whisker plots of the long-term annual mean dust mass path over the region 10°-20°N and 20°-30°W. Medians (red lines), interquartile range (blue boxes), the interquartile value +/- 1.25 times the interquartile range (black "whiskers") and outliers (red crosses) are calculated from annual mean dust mass path values over the period 1982–2004 (2000–2013 for the MODIS-Terra data). The model-averaged median mass path is 0.26 g m^{-2} (red line), which is a factor of three smaller than the satellite-derived dust mass path medians of 0.75 g m^{-2} (AVHRR) and 0.82 g m^{-2} (MODIS). Also shown (1b) is a scatterplot of annual mean DMP averaged over 10°-20°N and 20°-30°W (ordinate) and mean annual total dust emission from northern Africa (abscissa), for CMIP5 models (main plot) and the AVHRR and MODIS (inset), where error bars indicate the ± 1σ range of these data. Among the CMIP5 models the correlation coefficient of DMP and emission is 0.86 (p-value < 0.01) and the linear least square best fit line is $y = x \times 1.6e^{-4} + 0.05$ (red line), where the slope of the fit is statistically different from zero (p-value < 0.01). Annual mean dust emission values for the satellite data are estimated via this best-fit line.

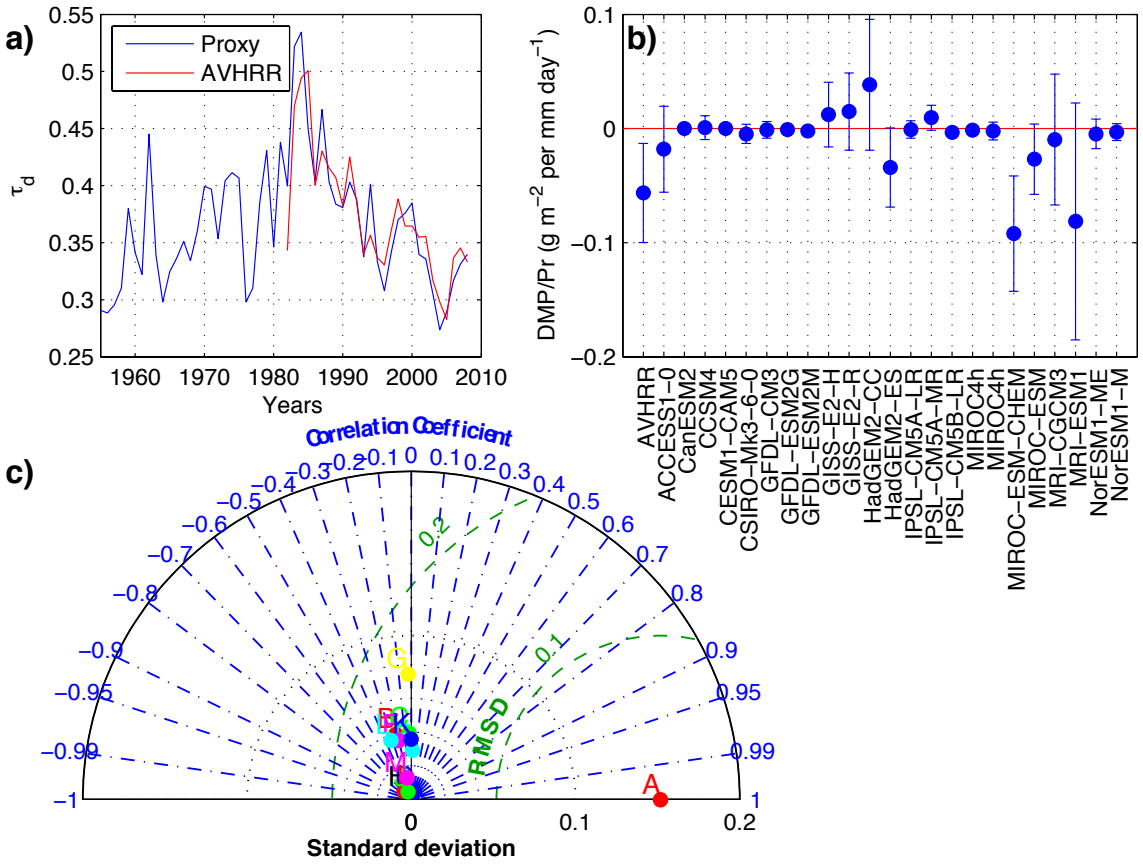

Figure 2. Annual variability of modeled and observed dust. Plotted in 3a are the proxy and AVHRR annual mean time series of τ_d averaged over 10°-20°N and 20°-30°W. Plotted in 3b are the coefficients (filled circles) and their 95% certainty levels (bars) from the regression of AVHRR and modeled DMP onto observed (for the AHVRR only) and modeled June–September Sahelian rainfall (10°-20°N and 15°W–20°E), calculated with data from 1960–2004. In 3c is a Taylor diagram for annual mean DMP for 1960–2004 and averaged over 10°-20°N and 20°-30°W. The red circle marked "A" represents the proxy record of DMP (3c), and the other markers are CMIP5 models (see Table S1 for legend). The abscissa and dotted black semi-circles represent the time series' standard deviation, the dashed green semi-circles are the root mean squared differences between the models and the proxy record, and the radial blue dot-dashed lines are the correlation coefficients of the model time series and the proxy record.

Supplementary Information

Supplementary Text
Supplementary References (30–35)
Table S1
Figures S1 & S2

Supplementary Text

Comparison of Dust emission source regions

While there are no observation-based maps of dust emission (units of g m^{-2} per unit time), there does exist a satellite-based climatology of emission frequency covering northern Africa (30,31). Analysis of the output from a dust model that simulates emission over northern Africa (32,33) suggests that emission magnitude (mass) is directly proportional to the event frequency; regions with frequent dust storms also emit larger dust amounts. As such, we compare maps of the long-term mean dust emission from those CMIP5 models for which these data are available, with a satellite-based dust event frequency map (Fig S1). In order to focus on the spatial pattern of northern African dust emission, and to facilitate the comparison of emission (models) and frequency (observations), all data are normalized by the maximum value of emission (or frequency) such that the range of the data plotted on each map is zero to one.

With respect to dust emission, the models can be grouped into two categories, those with near uniform emission across most of northern Africa (CanESM, CSIRO, GFDL, MIROC, NorESM) and those where emission is dominated by a smaller number of highly active locations (ACCESS, HadGEM, MRI). The latter of these two groups is more consistent with the emission frequency from satellites (Fig S1). However, even among these three models showing a smaller number of highly active sources, the physical location of those sources is not consistent with the observations. The only point of agreement between most models and the satellite observations is the Bodélé depression as one of the most active dust sources (34). We note that the satellite-based emission frequency may underestimate the number of dust events in the Saharan Heat Low (10°-20°N & 10°W-10°E) and within Western Sahara and coastal Mauritania (35). However, these possible biases do not explain the wide disparity in the spatial pattern of emission between the CMIP5 models and the observations.

20^{th} Century historical forcing Taylor Diagram

One feature of the Taylor diagram in Figure S2, which is constructed from the output of the 20^{th} Century historical forcing runs and the proxy dust time series in Figure 2a, are the low correlation coefficients between the observational data (A) and the models (B–W; legend in Table S1), where more than half of the models have negative correlations with the observations; the median correlation coefficient is -0.04 (Fig S2). Although three of the models exhibit statistically significant and positive correlation coefficients, ACCESS, Cam4 and MRI-CGCM3, the r^2 values for these models are very low (0.09, 0.09 and 0.11, respectively). We note that only one ensemble member of the DMP data was available for six of the 23 models used (Table S1), and that inclusion of more ensemble members in the analysis could, in theory, improve the results of the comparison to the observational data in Figure S2.

Supplementary References

30. Schepanski, K., I. Tegen, B. Laurent, B. Heinold, and A. Macke (2007), A new Saharan dust source activation frequency map derived from MSG-SEVIRI IR-channels, Geophys. Res. Lett., 34, L18803, doi:10.1029/2007GL030168.
31. Schepanski, K., I. Tegen, and A. Macke (2012), Comparison of satellite based observations of Saharan dust source areas, Remote Sens. Environ., 123, 90–97, doi:10.1016/j.rse.2012.03.019.
32. Fiedler, S., K. Schepanski, B. Heinold, P. Knippertz, and I. Tegen (2013), Climatology of nocturnal low-level jets over North Africa and implications for modeling mineral dust emission, J. Geophys. Res. Atmos., 118, 6100–6121, doi:10.1002/jgrd.50394.
33. Fiedler, S., Schepanski, K., Knippertz, P., Heinold, B., & Tegen, I. (2013). How important are cyclones for emitting mineral dust aerosol in North Africa?. Atmospheric Chemistry and Physics Discussions, 13(12), 32483-32528.
34. Kocha, C., P. Tulet, J.-P. Lafore, and C. Flamant (2013), The importance of the diurnal cycle of Aerosol Optical Depth in West Africa, Geophys. Res. Lett., 40, 785–790, doi:10.1002/grl.50143.
35. Brindley, H., P. Knippertz, C. Ryder, and I. Ashpole (2012), A critical evaluation of the ability of the Spinning Enhanced Visible and Infrared Imager (SEVIRI) thermal infrared red-green-blue rendering to identify dust events: Theoretical analysis, J. Geophys. Res., 117, D07201, doi:10.1029/2011JD017326.

Table S1

Centers	Model name	DMP/Fig S3 Key (kg/m2)	Fine AOD	Emission (kg m^{-2} s^{-1})	AMIP DMP Fig 2c Key
Commonwealth Scientific and Industrial Research Organisation (CSIRO) Bureau of Meteorology (BOM; Australia)	ACCESS1-0	***A***	-	X	A
National Center for Atmospheric Research (NCAR; United States)	CCSM	***B***	-	-	B
Canadian Centre for Climate Modelling and Analysis (CCCma; Canada)	CanESM2	***C***	-	X	C
National Science Foundation (NSF)–Department of Energy (DOE)–NCAR (United States)	CESM	D	-	-	D
CSIRO–Queensland Climate Change Centre of Excellence (QCCE; Australia)	CSIRO-Mk3-6-0	***E***	X	X	E
National Oceanic and Atmospheric Administration (NOAA)/Geophysical Fluid Dynamics Laboratory (GFDL; United States)	GFDL-CM3	***F***	X	X	-
	GFDL-ESM2G	G	X	-	-
	GFDL-ESM2M	H	X	-	-
National Aeronautics and Space Administration (NASA)–Goddard Institute for Space Studies (GISS; United States)	GISS-E2-H	***I***	-	-	-
	GISS-E2-R	***J***	-	-	-
Met Office Hadley Centre (MOHC; United Kingdom)	HadGEM2-A	-	-	-	F
	HadGEM2-CC	***K***	-	X	-
	HadGEM2-ES	***L***	-	X	-
L'Institut Pierre-Simon Laplace (IPSL; France)	IPSL-CM5A-LR	***M***	X	-	G
	IPSL-CM5A-MR	***N***	X	-	H
	IPSL-CM5B-LR	O	X	-	I
Model for Interdisciplinary Research on Climate (MIROC; Japan)	MIROC4h	***P***	-	X	-
	MIROC5	***Q***	-	X	J
	MIROC-ESM-CHEM	R	X	X	-
	MIROC-ESM	***S***	X	X	-
Meteorological Research Institute (MRI; Japan)	MRI-CGCM3	***T***	X	X	K
	MRI-ESM1	***U***	X	X	-
Norwegian Climate Centre (NCC; Norway)	NorESM1-ME	V	-	X	-
	NorESM1-M	***W***	-	X	L

Table S1. Description of CMIP5 model data used in this study. Listed by column, from left to right, are the model centers, the model names, letter corresponding to the model's location in Figure S2 (where bold indicates if ensemble means were available for the historical forcing experiment), if fine mode τ output was available for the historical forcing experiment (indicated by an X), if emission output was available for the historical forcing runs, and letter corresponding to the model's location in Figure 2c (for the AMIP experiments).

Figure S1

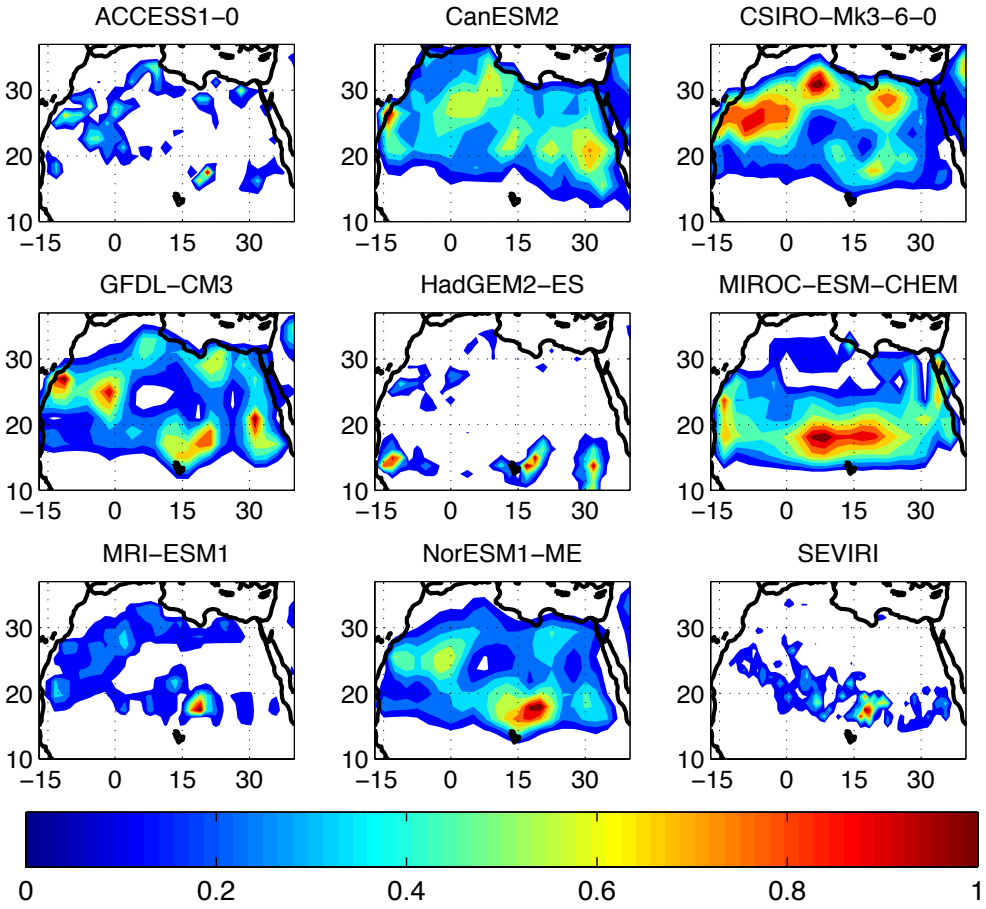

Figure S1. Modeled surface dust emission and comparison to satellite data. Shown are maps of the normalized (divided by the maximum value) surface dust emission from eight models. Regions plotted white are not active while those in red are the most active. Also shown (bottom right) is the normalize dust frequency map derived from the MSG-SEVIRI instrument.

Figure S2

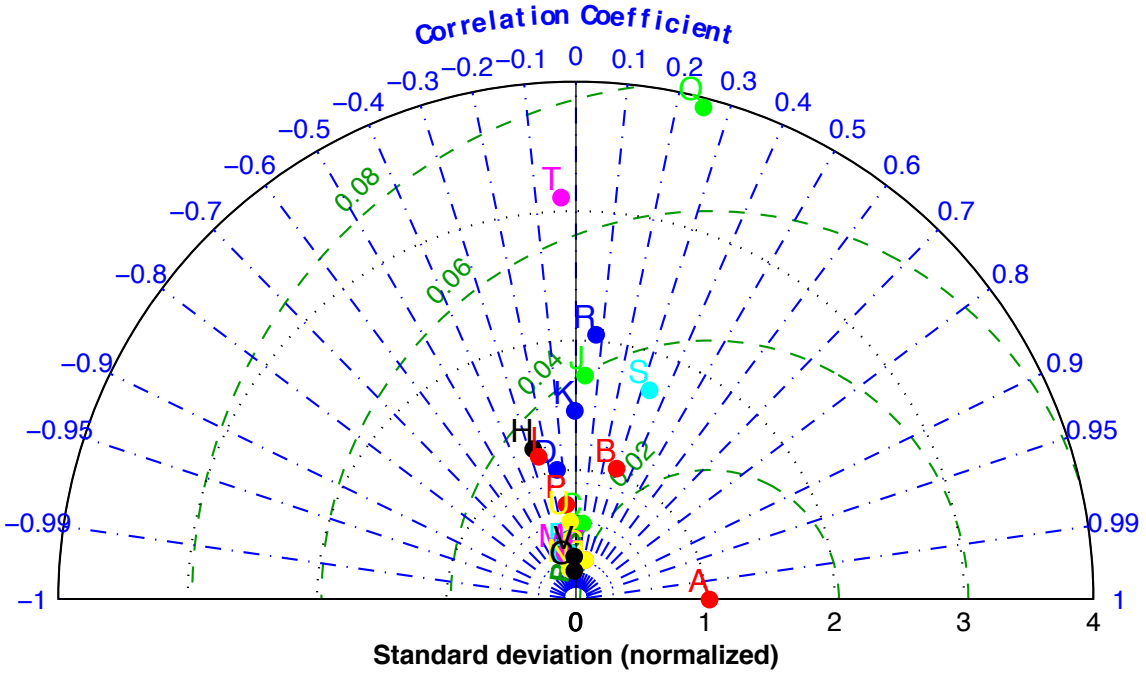

Figure S2. Taylor Diagram of dust mass path over Cape Verde. Shown is a Taylor diagram for annual mean DMP over the Cape Verde islands for the time period 1960–2005 (Fig 2a). The red circle marked "A" represents the proxy record of dust, and the other markers are CMIP5 models (see Table S2 for legend). The abscissa and dotted black semi-circles represent the time series' standard deviation, normalized such that the proxy record has a standard deviation of unity. The dashed green semi-circles are the root mean squared differences between the models and the proxy record, and the radial blue dot-dashed lines are the correlation coefficients of the model time series and the proxy record.